Validation of ICON-MIGHTI thermospheric wind observations: 2. Green-line comparisons to specular meteor radars

Brian J. Harding[1], Jorge L. Chau[2], Maosheng He[2], Christoph R. Englert[3], John M. Harlander[4], Kenneth D. Marr[3], Jonathan J. Makela[5], Matthias Clahsen[2], Guozhu Li[6,7], M. Venkat Ratnam[8], S. Vijaya Bhaskar Rao[9], Yen-Jung J. Wu[1], Scott L. England[10], Thomas J. Immel[1]

[1]Space Sciences Laboratory, University of California, Berkeley, California, USA
[2]Leibniz Institute of Atmospheric Physics at the University of Rostock, Kühlungsborn, Germany [3]Space Science Division, U.S. Naval Research Laboratory, Washington, D.C. , USA
[4]Space Systems Research Corporation, Alexandria, Virginia, USA
[5]Department of Electrical and Computer Engineering, University of Illinois at Urbana-Champaign, Urbana, IL, USA
[6]Beijing National Observatory of Space Environment, Institute of Geology and Geophysics, Chinese Academy of Sciences, Beijing, China
[7]College of Earth and Planetary Sciences, University of Chinese Academy of Sciences, Beijing, China
[8]National Atmospheric Research Laboratory, Tirupati, India
[9]Department of Physics, Sri Venkateswara University, Tirupati, India
[10]Department of Aerospace and Ocean Engineering, Virginia Polytechnic Institute and State University, Blacksburg, VA, USA

Key Points:

- Coincident wind measurements by ICON-MIGHTI and specular meteor radars are strongly correlated (r=0.82)
- The mean discrepancy between the datasets is 4.5 m/s, validating the MIGHTI v03 zero reference
- The RMS discrepancy is 26 m/s, which is attributed to inherent data errors and variability on time scales $\lesssim$ 70 min

Corresponding author: Brian J. Harding, `bharding@ssl.berkeley.edu`

Abstract

We compare coincident thermospheric neutral wind observations made by the Michelson Interferometer for Global High-Resolution Thermospheric Imaging (MIGHTI) on the Ionospheric Connection Explorer (ICON) spacecraft, and four ground-based specular meteor radars (SMRs). Using the green-line MIGHTI channel, we analyze 1158 coincidences between Dec 2019 and May 2020 in the altitude range from 94 to 104 km where the observations overlap. We find that the two datasets are strongly correlated (r=0.82) with a small mean difference (4.5 m/s). Although this agreement is good, an analysis of known error sources (e.g., shot noise, calibration errors, and analysis assumptions) can only account for about a quarter of the disagreement variance. The unexplained variance is 27.8% of the total signal variance and could be caused by unknown errors. However, based on an analysis of the spatial and temporal averaging of the two measurement modalities, we suggest that some of the disagreement is likely caused by temporal variability of the wind on scales $\lesssim$70 min. The observed magnitudes agree well during the night, but during the day, MIGHTI observes 16–25% faster winds than the SMRs. This remains unresolved but is similar in certain ways to previous SMR-satellite comparisons.

Plain Language Summary

Although Earth's atmosphere becomes less dense at high altitudes where it transitions to space, the wind speed grows faster, often exceeding 100 m/s (225 mph). One barrier to better predictions of conditions in the near-Earth space environment is obtaining knowledge of the wind in the thermosphere, the uppermost layer of the atmosphere. Measurements of the thermospheric wind are difficult to make and historically sparse. ICON, a new NASA mission launched in October 2019, carries the MIGHTI instrument to measure the wind from 90 to 300 km altitude. In this study we compare the observations of MIGHTI to those of meteor radars, which measure the wind from the ground by analysis of radio waves reflected by meteor trails. The results indicate good agreement between the datasets when they measure the wind at the same time and place. Specifically, with 1158 coincidences over the first 6 months of the ICON mission, the correlation is 0.82 and and the average difference is 4.5 m/s. This study is important because it validates the MIGHTI data, giving confidence for subsequent studies using its data. It also quantifies limits to the agreement between space-based and ground-based winds, which is useful information for future studies combining them.

1 Introduction

The thermospheric wind acts to distribute energy and momentum from high-latitude drivers to the global thermosphere-ionosphere system, and likewise from sources in the lower and middle atmosphere to near-Earth space. In the lower thermosphere, a region with high electrical conductivity, neutral winds generate dynamo electric fields which transport ionospheric plasma (Heelis, 2004; Richmond, 2011). In the upper thermosphere, winds force the ionosphere via drag and via advection of compositional changes (Rishbeth, 1972). The interplay between these and other wind-driven processes is not well understood but is critical for predicting variability in the thermosphere-ionosphere system (Pedatella et al., 2018; Liu, 2016; Maute et al., 2012; Fuller-Rowell, 2011; England, 2011; Titheridge, 1995; Killeen, 1987). However, the thermospheric wind is difficult to observe, and measurements remain sparse.

A new wind dataset is now available from the Ionospheric Connection Explorer (ICON), a NASA mission launched in October 2019 to study the sources of ionospheric variability (Immel et al., 2017). The Michelson Interferometer for Global High-Resolution Thermospheric Imaging (MIGHTI) is one of four instruments on-board ICON (Englert et al., 2017), measuring the low-/mid-latitude horizontal wind between 90 and 300 km altitude. Wind estimates are derived from remote observations of Doppler shifts in two naturally occurring atomic oxygen airglow emissions: the green line (the $O(^1S\text{–}^1D)$ 557.7-nm emission in the lower thermosphere) and the red line (the $O(^1D\text{–}^3P)$ 630.0-nm emission in the middle/upper thermosphere). In addition to the neutral wind, MIGHTI also measures neutral temperature by observing the spectral shape of the O_2 A-band emission (Stevens et al., 2018). In this study we focus on MIGHTI wind observations obtained from the green line.

Although different interferometric techniques were used, similar wind observations were made by previous space-borne instruments: for example, the Fabry-Perot interferometer on Dynamics-Explorer 2 (DE-2) (Hays et al., 1981), the Wind Imaging Interferometer (WINDII) (Shepherd et al., 2012) and the High-Resolution Doppler Imager (HRDI) (Hays et al., 1993) on the Upper Atmosphere Research Satellite (UARS), and most recently the Thermosphere Ionosphere Mesosphere Energetics and Dynamics (TIMED) Doppler Interferometer (TIDI) (Killeen et al., 2006). MIGHTI is unique in that it gathers data from both OI emissions and all altitudes simultaneously, with no duty cycling or scanning of the field of view or interferometer parts. Although this is an advantage for data coverage and cadence, it requires that separate calibrations be employed for each sensor, wavelength, and altitude. Thus, validation is critical.

Other methods to measure the thermospheric wind include observing the red and green emissions from the ground (Meriwether, 2006), tracking satellite drag (Xiong et al., 2015; Visser et al., 2019), observing the drift of tracers released from sounding rockets (Larsen, 2002), inverting incoherent scatter drifts in the lower thermosphere (Hysell et al., 2014), and observing the Doppler shift of specular radar echoes from meteor trails (Chau et al., 2019). The specular meteor radar (SMR) method has the advantage of continuous temporal coverage, with altitude coverage reaching from below the mesopause to $\sim$105 km or higher. It is thus a promising method for validation of MIGHTI green-line winds, which have complete local time coverage spanning 90–$\sim$109 km. A separate paper discusses validation of the MIGHTI nighttime red-line winds by comparing with ground-based Fabry-Perot interferometers (Makela et al., 2020).

Although validation is the primary goal, understanding and quantifying the differences between these two techniques is useful in other ways. In general, ground-based sensors have excellent local-time coverage but poor spatial coverage, while space-based sensors have global-scale spatial coverage, but poor local-time coverage (as controlled by orbital precession which takes weeks or months). Combining these sampling strategies could be advantageous for quantifying the spatiotemporal variability of the thermosphere. The quantitative comparisons shown here are useful for identifying any cross-calibration issues and also for tuning assimilative models. Finally, since MIGHTI and SMR have similar horizontal and vertical spatial resolutions (as discussed in the Appendix) but different temporal resolutions, statistical differences in the two observations are potentially a measure of wind variability on time scales $\lesssim$70 min.

2 Instrumentation

In this study we compare observations made by MIGHTI and by a SMR at nearly the same place and time, which we refer to as a coincidence. An idealized MIGHTI-SMR coincidence is shown schematically in Figure 1, indicating the locations of ICON, the MIGHTI lines of sight, the green line airglow layer, and a representative set of meteor detections. More details on MIGHTI and SMR wind observations are described below.

2.1 ICON-MIGHTI

MIGHTI utilizes the Doppler Asymmetric Spatial Heterodyne (DASH) spectroscopy technique (Harlander et al., 2017) to sense Doppler shifts in the red line and green line emissions. From a 27° inclination orbit at $\sim$600 km altitude, the two MIGHTI sensors

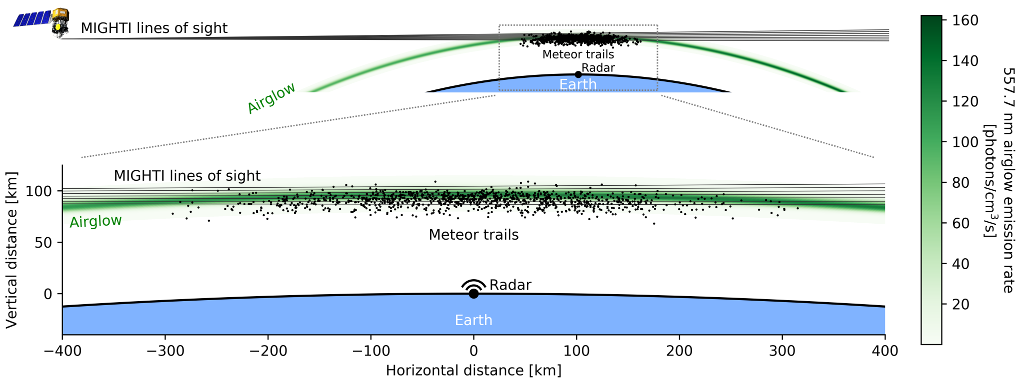

Figure 1. The geometry of a coincidence between ICON-MIGHTI and a specular meteor radar (SMR). Black dots indicate meteor detections during a 71-minute period (the full-width half-max of the temporal weighting used in the SMR analysis). Black lines indicate the six lowest MIGHTI lines of sight. An average 557.7 nm green line airglow distribution is shown, for the night case. During the day, the emission layer is thicker. The bottom graphic is shown to scale, and in the top graphic the vertical coordinate is stretched by a factor of 2.

observe the northern limb at azimuth offsets of 45° and 135° from the spacecraft velocity vector, covering latitudes from about 12°S to 42°N. For each exposure from each sensor, the observed interferogram is inverted to estimate the component of the horizontal neutral wind along MIGHTI's line of sight (LoS). Wind estimates are generally available continuously from 90–300 km altitude during the day, with a gap at night between ∼109 and ∼210 km, where the airglow is dim or nonexistent. More details of the wind retrieval are described by Harding et al. (2017).

The inverted wind speed profiles (i.e., the component of the horizontal wind vector in the direction of the field of view, as a function of altitude, hereafter "LoS wind profiles") are ICON's Level 2.1 data product. Profiles from the two orthogonally oriented sensors (MIGHTI-A and MIGHTI-B) are combined to estimate altitude profiles of the zonal and meridional wind, which is ICON's Level 2.2 data product. In normal science mode, MIGHTI-B observes the same region of the atmosphere as MIGHTI-A after 5–8 minutes of spacecraft motion. Combining these observations implicitly assumes the wind has not changed significantly over this period. In this study, we use the Level 2.1 data product, since no assumptions of temporal coherence are needed, and it will allow us to separately investigate the calibrations of the two MIGHTI sensors.

The vertical sampling of MIGHTI is 2.9 km on the limb at 90 km altitude, and 2.2 km at 300 km altitude. MIGHTI takes an exposure every 30 seconds in day mode and 60 seconds in night mode. As a result of spacecraft motion, this implies a horizontal averaging of ∼250 or 500 km in the along-track direction. In addition, the long path of the LoS through the emitting layer represents a horizontal averaging of hundreds of km, where deviations from the assumption of spherical symmetry have the potential to incur retrieval errors (Y. J. Wu et al., 2020). The Appendix contains a detailed quantification of horizontal resolution issues in MIGHTI and SMR. In brief, at night the MIGHTI horizontal sampling is similar to or slightly larger than the horizontal sampling of the SMR. During the day, the MIGHTI sampling is a factor of 3–4 larger since the emission layer is thicker.

For any interferometric velocity measurement, determination of the zero reference is a critical calibration step. For the MIGHTI v03 dataset used in this study, the zero

Table 1. Specular meteor radar sites

Name	Latitude	Longitude	Frequency	Peak power	Reference
Tirupati	13.6°N	79.4°E	35.25 MHz	40 kW	Rao et al. (2014)
Ledong	18.4°N	109.0°E	38.9 MHz	20 kW	Wang et al. (2019)
Wuhan	30.5°N	114.6°E	38.9 MHz	20 kW	Yu et al. (2013)
Beijing	40.3°N	116.2°E	38.9 MHz	10 kW	Yu et al. (2013)

wind phase was established by a comparison between a 60-day average of MIGHTI data and a 60-day average of the Horizontal Wind Model 2014 (Drob et al., 2015), an empirical model informed by decades of previous wind measurements. Separate calibrations are used for MIGHTI-A and -B, red and green, day and night, and for each row of pixels on the detector (i.e., each altitude). A future release will utilize the on-orbit zero-wind maneuver to refine this calibration. More information on the latest release can be found in the MIGHTI documentation (`ftp://icon-science.ssl.berkeley.edu/pub/Documentation/`).

2.2 Specular Meteor Radar (SMR)

In this work we use four monostatic SMRs located at Tirupati, Ledong, Wuhan and Beijing, spanning from low to mid latitudes. The SMRs are from the same manufacturer, and each uses one single antenna on transmission and five antennas on reception in an interferometer configuration. The latter is used to locate the scattering center of the received echo, which along with the measured LoS Doppler velocity, is used to get horizontal winds using the homogeneous velocity technique over the illuminated area (around 180 km radius at 90 km altitude) (e.g., Holdsworth et al., 2004). These winds have been obtained by binning the meteor measurements in time and altitude using a Gaussian weighting function with total widths, i.e., 2σ, of one hour and two km in time and altitude, respectively. The location, frequency, peak transmitter power and selected reference for each of the four radars can be found in Table 1.

The horizontal velocity in each bin is obtained using a least square fitting procedure with at least ten detections after data selection. The data selection process consists of selecting detections with elevation angles greater than 30 degrees to avoid large uncertainties in altitude, and removing detections with Doppler velocities larger than 3σ deviations, where σ is estimated from daily distributions of radial velocities. Typical values of σ are 35–50 m/s. The same analysis software is used for all four sites.

3 Results and Discussion

We use the first 6 months of MIGHTI LoS wind data, from 2019-12-06 (the start of routine science mode) to 2020-05-31. We only use samples for which the “wind quality factor” is equal to 1 (i.e., highest quality). For each SMR site, we consider all coincidences, namely, times when the MIGHTI tangent point passes within a horizontal distance of 300 km from the SMR site. This threshold was chosen to be consistent with the distance traversed by the line of sight through the tangent altitude shell and roughly consistent with the MIGHTI horizontal resolution (see Appendix), but our qualitative conclusions do not change when different reasonable thresholds are used. This results in a dataset of 1158 coincidences, spanning a variety of dates and local times. In order to compare with the MIGHTI LoS wind, the meteor radar wind vector is projected onto the MIGHTI viewing direction. In normal science mode, this is a direction between North and East for MIGHTI-A and between West and North for MIGHTI-B, depending on latitude.

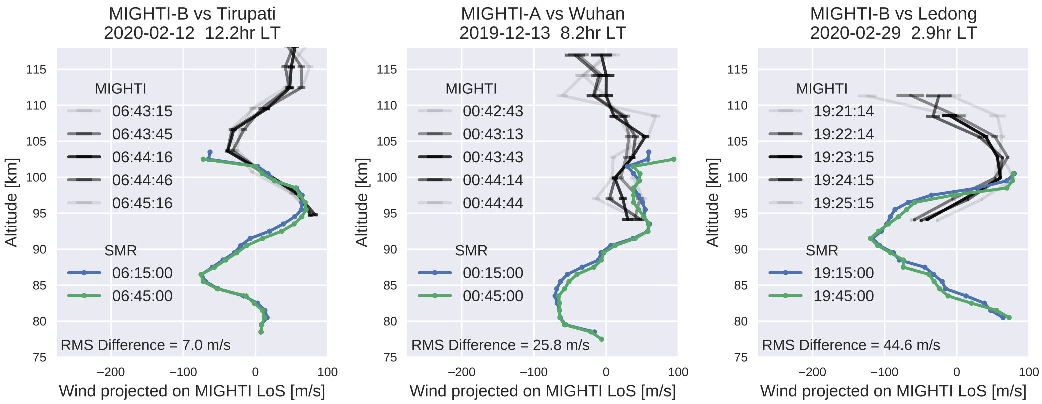

Figure 2. Three examples of coincident wind observations from ICON-MIGHTI and from specular meteor radars (SMRs). Colored lines are the SMR profiles before and after the coincidence, projected onto the MIGHTI line of sight (LoS) vector. Black lines are consecutive MIGHTI LoS wind profiles (ICON data product 2.1) during the overflight, where the transparency represents the horizontal distance to the SMR site. In all three cases, the closest approach is less than 85 km. Error bars represent 1σ statistical errors. The root-mean-square (RMS) difference between the MIGHTI and SMR profiles is also displayed.

3.1 Individual coincidences

Figure 2 shows three example coincidences, which represent good, average, and poor agreement. In terms of the root-mean-square (RMS) difference (calculated in the altitude region where the datasets overlap), the left panel is 7.0 m/s, the middle panel is 25.8 m/s and the right panel is 44.6 m/s, which is in the 7th, 59th, and 92nd percentile, respectively, among all coincidences with at least 3 overlapping altitude samples. In each panel, two SMR wind profiles are shown in color, corresponding to the two time intervals centered before and after the coincidence. MIGHTI wind profiles during the overflight are shown in black, where the transparency of the line is proportional to the horizontal distance from the SMR site.

In a qualitative sense, the MIGHTI wind profile and the SMR profile have similar trends with altitude. The structure is dominated by a vertical wavelength of 10–20 km, consistent with tides. Where the MIGHTI and SMR profiles overlap, they display similar slopes. However, in some cases the observations differ by 50 m/s or more. These differences are larger than the difference between the two consecutive SMR profiles, and are usually larger than the differences in 5 consecutive MIGHTI profiles during the pass. This suggests that the MIGHTI-SMR disagreements cannot be attributed to statistical noise in either instrument, as we discuss further in Section 3.4. In the next section we analyze all 1158 coincidences to make a more quantitative comparison.

3.2 Statistics

For each of the 1158 MIGHTI overflights of a SMR site, we consider only the closest MIGHTI exposure, and linearly interpolate the SMR data in time and altitude to the MIGHTI time and altitudes. This interpolation is not expected to generate a significant error, because the SMR profiles are generally smooth in time and space (i.e., altitude and time variations are dominated by the true signal, not white noise). Extrapolation is never used.

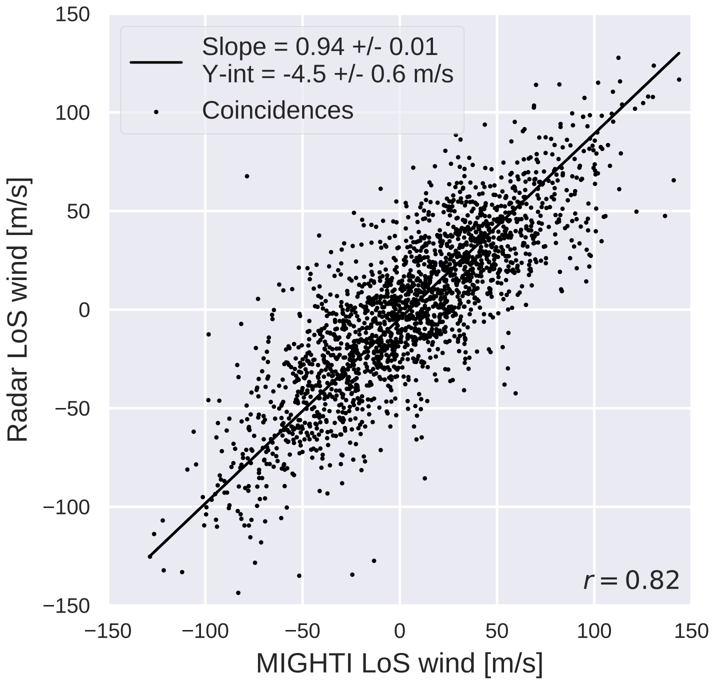

Figure 3. Summary of 1158 coincidences between MIGHTI and four SMR sites. Each dot indicates one altitude from one coincidence, spanning dates from Dec 2019 to May 2020 and altitudes from 94 to 104 km. Cardinal winds from the SMR observation are interpolated to the MIGHTI sample locations and projected onto MIGHTI's line of sight (LoS). The Pearson correlation is 0.82. A linear fit using orthogonal distance regression is also shown, with a slope of 0.94 and a mean offset of -4.5 m/s. Standard error of the slope and y-intercept estimates are also shown.

Depending on meteor density, SMR winds overlap with up to 4 MIGHTI altitude samples on each coincidence. In total, 2054 data points are available from the 1158 coincidences, spanning ∼94 to ∼104 km. MIGHTI observes two lower altitudes as well (∼88 and ∼91 km). However, they are not included in this study because they are currently labeled with a quality of 0.5 (i.e., "caution") pending a more detailed analysis of the calibrations for these rows near the edge of the field.

Figure 3 compares the MIGHTI wind to the SMR wind, where each point represents one altitude from one coincidence. A linear fit using orthogonal distance regression is also shown. The correlation between the two datasets is 0.82, implying that 67% of the observed signal variance is common between MIGHTI and the SMRs. The slope of the fit (0.94) is near 1, suggesting that similar wind magnitudes are seen between the two datasets. The fact that the slope is slightly less than 1 is discussed in more detail below.

Taking the difference (MIGHTI wind minus SMR wind), which is hereafter referred to as the "discrepancy," we find that the mean discrepancy is 4.5 m/s. Since the same local oscillator is used for transmission and reception, the SMR zero baseline is many orders of magnitude more accurate than the MIGHTI zero baseline, and this result is thus interpreted as a validation of the zero wind reference used in the MIGHTI v03 dataset. The RMS discrepancy is 26.4 m/s. Overall, this result gives confidence that MIGHTI is healthy and providing useful green-line wind data in its first 6 months of operation.

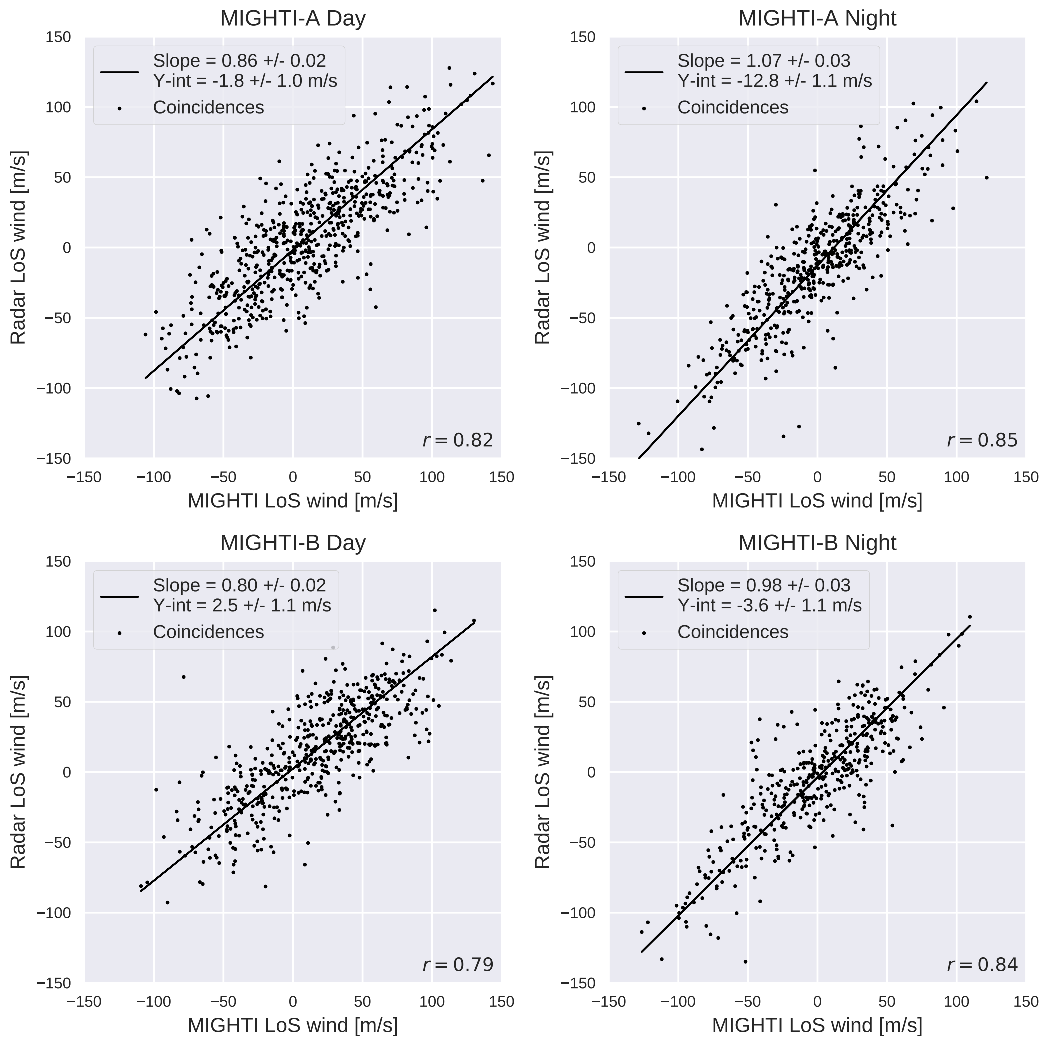

Figure 4. Same as Figure 3, except the dataset is split between the two MIGHTI sensors and between the two MIGHTI operating modes (Day and Night).

3.3 Day/night differences

No trends are apparent when the MIGHTI-SMR discrepancy is analyzed as a function of altitude, coincidence distance, viewing direction, ascending/descending orbit, date, or SMR site. However, one difference is clear when the discrepancy is analyzed separately in day mode and night mode. Figure 4 shows the same data as Figure 3 except the dataset is split into 4 subsets, separating MIGHTI-A/B and day/night mode. In day mode, the exposure is 30 sec instead of 60 sec, the aperture is stopped to 15% of the nighttime aperture, and the emission layer spans more altitudes. Separate calibrations for zero wind, visibility, flat field, and phase distortion are used for these 4 cases, so it is useful to analyze them independently.

In all 4 cases in Figure 4, we find similar values for the RMS discrepancy (23.7 – 27.8 m/s) and the correlation (0.79 – 0.85). The mean offsets are negligibly small (1.8, 2.5, and 3.6 m/s) with the exception of MIGHTI-A in night-mode, which is 12.8 m/s. This could be caused by an inaccuracy in the Horizontal Wind Model or by uncorrected mechanical shifts, and this case will be a focus of an updated zero wind calibration for a future MIGHTI data release.

One striking feature of Figure 4 is the apparent difference in fitted slopes between day mode and night mode. In night mode the slopes are 1.07 and 0.98, while in day mode they are consistently smaller (0.86 and 0.80). In other words, in day mode MIGHTI-A measures 16% faster winds and MIGHTI-B measures 25% faster winds than the SMRs.

The cause of this disagreement is not presently known. It is interesting to note that similar features were seen in previous comparisons between space-based and SMR-based winds. Burrage et al. (1996) compared the HRDI O_2(0-0) winds to the Jakarta SMR. They did not quantify the correlation, but reported that HRDI measured generally larger meridional winds than the SMR. Forbes et al. (2004) compared HRDI O_2(0-0) winds to three SMRs in terms of zonal-mean winds and retrieved tidal amplitudes. One conclusion of this study was a multiplicative speed bias of 1.6 for zonal-mean winds and 1.3 for the semidiurnal tide. An anisotropy was noted wherein the zonal winds disagree more than the meridional winds. Finally, Q. Wu et al. (2006) reported a larger diurnal tide amplitude in TIDI O_2(0-0) meridional wind data than in SMR data from Maui. While it is probable that multiple factors are contributing to these conclusions, it is noteworthy that all these studies found space-based winds to be faster than ground-based winds in certain ways. To our knowledge, no study reached the opposite conclusion.

We performed an identical analysis (not shown here) using the MIGHTI cardinal wind data (ICON data product 2.2) compared to the SMR cardinal wind data, and no significant difference between zonal and meridional wind comparisons were found. This is expected given that the cardinal wind data is a combination of MIGHTI-A and -B data, and no significant difference between MIGHTI-A and -B is seen in the LoS wind comparisons.

To our knowledge the root cause of previous ground-to-space discrepancies has not been identified. The MIGHTI-SMR comparisons shown here are qualitatively consistent with previous comparisons and suggest an inherent bias with SMR wind observations or with space-borne airglow-based wind observations. Our study suggests this problem may exist in the daytime only. As the biggest difference between day and night is the thickness of the airglow layer, this suggests some influence of error from the inversion of the space-based measurement. One possibility arises from the fact that the MIGHTI samples used here are taken from the bottom of the green-line airglow profile. As a consequence of the inversion, the retrieved wind at these low altitudes is a small difference of large numbers and is thus sensitive to small errors in flat fielding or violations of spherical symmetry (Y. J. Wu et al., 2020). This will be a focus of future work. Until this disagreement is resolved, users of MIGHTI data could take a conservative approach by evaluating the impact of a 16–25% positive daytime speed bias on their conclusions. Although this disagreement could be important for certain analyses, the winds are not usually large enough for this to significantly contribute to the total RMS discrepancy of 26.4 m/s. Other factors must be dominant. We discuss possible contributors to the discrepancy in the next section.

3.4 Sources of Discrepancy

The results shown above are interpreted as validation of the first 6 months of MIGHTI's green-line winds, in terms of the variations and the zero baseline for both operating modes and both sensors. However, even though the MIGHTI-SMR discrepancy is small, it is not negligible, and it is important to understand for future studies. Notably, the discrepancy cannot be understood simply as noise in the data. The mean precision (i.e., random or statistical error) in the MIGHTI data used in these comparisons is 3.3 m/s and in the SMR winds is <1 m/s. Even if the reported precision values were optimistic by a factor of 2, which is unlikely, the noise variance would remain less than 7% of the dis-

Table 2. Sources of discrepancy in MIGHTI-SMR comparisons with estimated magnitudes

Source	**Root-mean-square magnitude**	**Percent variance**
LoS wind measurements	43.3 m/s	
MIGHTI-SMR discrepancy	26.4 m/s	100.0%
MIGHTI shot and read noise	3.3 m/s	1.6%
MIGHTI mechanical drift	5 – 10 m/s	3.6 – 14.4%
MIGHTI zero wind error	4.9 m/s	3.4%
MIGHTI spherical asymmetry	<5 m/s	<3.4%
SMR precision	<1 m/s	< 0.14%
SMR sensitivity to gradients	3.5 m/s	1.8%
SMR sensitivity to vertical wind	1.4 m/s	0.3%

crepancy variance. For future studies utilizing MIGHTI data, and possibly combining them with SMRs, there is a need to understand other factors contributing to the discrepancy.

In the following, we discuss possible factors, which are summarized in Table 2. For each factor, an estimate of the RMS magnitude is provided, as well as the square of that quantity, reported as a percent of the discrepancy variance.

Although statistical errors are small, there can be errors in calibration or assumptions in the analysis. For MIGHTI, there are two possibilities for calibration errors: instrument drift and zero wind error. As discussed above, the zero wind error is estimated at 4.8 m/s. Instrument drift is dominated by thermal fluctuations in the interferometer and in the mechanical alignment. Interferometer drift is corrected by monitoring the interference fringes of an on-board calibration lamp (Marr et al., 2019); an error in this correction cannot be ruled out, but since the observed variation is slow and periodic with respect to the orbit, the correction is straightforward and unlikely to cause a significant error. Mechanical drift can be monitored using the position of a notch-pattern engraved on one of the interferometer gratings (Harlander et al., 2017; Englert et al., 2017; Marr et al., 2020). This correction is not implemented in v03 data but will be included in a future release. Its RMS magnitude is estimated at 5 – 10 m/s based on preliminary analysis.

Errors from spherical asymmetries in emission rate were investigated by Y. J. Wu et al. (2020), who predicted errors less than 5 m/s at 97 km. This error was concentrated in data near the terminators, which are automatically discarded in our analysis since they are labeled with a "wind quality factor" of 0.5 (i.e., caution) in the MIGHTI data product. However, we include 5 m/s as a worst case error. Errors in the inversion caused by spherical asymmetries in the wind are another possible source of error. Attempting to quantify this error would require accurate knowledge of small-scale fluctuations in the wind. Such analysis is not attempted here. Another possible concern regarding airglow gradients is the spacecraft velocity correction. The spacecraft velocity projected onto the LoS changes by 240 m/s from the left edge to the right edge of the 2.7° field of view. The data analysis corrects for spacecraft motion by adjusting the phase at each pixel independently (Harding et al., 2017), so even in cases of extreme horizontal or vertical airglow gradients, no systematic error is introduced.

One other possibility is an altitude registration error. Indeed, some of the individual coincidences (e.g., Figure 2, right panel) would appear to agree better if the MIGHTI profile were shifted up or down. Although meteor geolocation is expected to be accurate, the MIGHTI geolocation is dependent upon an analysis of star fields to register the field of view. This was achieved to a precision of 0.01° or ∼0.2 km on the limb. We performed an analysis of the MIGHTI-SMR coincidences using different offsets for MIGHTI pointing, and found that the optimal offset is to shift the MIGHTI profile down by 1–2 km, where the discrepancy is reduced by 0.8 – 1.4 m/s. This improvement is small relative to the 26.4 m/s discrepancy, and the optimal shift is smaller than the field of view of an individual MIGHTI pixel, which is 2.2 – 2.9 km. Thus, we do not consider this effect further.

SMR data used in this study were processed assuming a horizontally homogeneous wind field and no vertical wind. If the meteor density were infinite, then the retrieved wind would indeed be a spatial average of the true wind (weighted by the averaging kernel, as described in the Appendix). However, a finite meteor density raises the possibility that high spatial frequencies of the wind may alias into the estimated wind. To test the impact of this assumption to first order, we reprocessed SMR data allowing for an estimate of gradients in zonal and meridional wind. The RMS difference was 3.5 m/s. Similarly, a test of the vertical wind sensitivity was performed, which led to an RMS difference of 1.4 m/s.

Assuming the errors are independent and add in quadrature (i.e., the variances add linearly), and using worst-case values, we conclude that 25% (13.2 m/s RMS) of the discrepancy variance can be explained by known instrument errors. The remaining discrepancy (75% or 22.8 m/s RMS) must be caused by either an unknown major error source or by the different MIGHTI and SMR averaging kernels, or some combination. The MIGHTI and SMR data are measured at nearly the same time and place, with nearly the same vertical averaging (∼2–3 km), and horizontal averaging functions with similar widths (see Appendix; MIGHTI's averaging is slightly larger during the night and 3–4 times larger during the day).

However, their temporal averaging is vastly different. As mentioned above, the SMR analysis averages using Gaussian weighting with $2\sigma = 60$ min (i.e., full-width at half-maximum of 71 min), while MIGHTI's exposure time is 0.5 min (day mode) or 1 min (night mode). Thus, the remaining discrepancy could be resolved if temporal scales $\lesssim$70 min contain 27.8% of the total kinetic energy of the wind between 94 and 104 km.

A correlation analysis was performed and finds a Pearson correlation of 0.53 between the discrepancy at ∼94 km and at ∼97 km, and likewise a correlation of 0.54 between ∼97 km and ∼100 km. Such a feature is not expected to result purely from statistical noise (which would be nearly uncorrelated between rows) nor from calibration errors (which would be nearly correlated between rows). However, it is consistent with gravity waves with finite vertical wavelengths, and it supports the notion that much of the discrepancy could be related to wind fluctuations on short time scales. The data used here cannot disambiguate the effects of gravity wave variance and unknown data errors. Quantifying the contribution to variability from waves with short time scales could be possible with incoherent scatter based wind estimates (Hysell et al., 2014) or with correlation analysis of multistatic meteor radar data (Vierinen et al., 2019). Users of MIGHTI data wishing to take a conservative approach could attribute all of the unexplained discrepancy to MIGHTI, thus defining an upper bound for MIGHTI error of 26.4 m/s RMS.

4 Conclusion

We have compared simultaneous and colocated thermospheric wind measurements in the 94 – 104 km altitude range from two sources: the ICON-MIGHTI v03 dataset and four SMRs. By comparing 1158 coincidences when MIGHTI observes the atmosphere over the SMR site, we find strong correlation (r=0.82) with small mean offset (4.5 m/s). This is interpreted as a successful validation of the initial 6 months of MIGHTI's green-line data, in terms of both the MIGHTI zero reference and variations about that reference. The RMS difference in the two observations is 26.4 m/s, which is a small but significant discrepancy. Only about a quarter of this discrepancy can be attributed to known instrument errors like shot noise, calibrations, or assumptions in the analysis. The remaining discrepancy (22.8 m/s RMS) could be caused by some combination of unknown errors or wind fluctuations on time scales $\lesssim$70 min. No trends in the discrepancy are seen with altitude, coincidence distance, viewing angle, ascending/descending orbit, date or SMR site; however, one difference is apparent between day mode and night mode. In day mode, MIGHTI observes 16–25% faster winds than the SMRs, an artifact which appears to be consistent in some ways with historical SMR versus satellite limb comparisons but remains unresolved and will be a focus of future work. Our results are a necessary validation of green-line (lower thermospheric) MIGHTI winds, and they provide a quantitative context for future work that will combine space-based and ground-based winds for characterizing the spatiotemporal variability of the lower thermosphere.

Appendix A Horizontal Resolution

In the following, we compute the horizontal resolution of MIGHTI and SMR, showing that they are comparable at night (with MIGHTI slightly larger) but different by a factor of 3–4 during the day. This result is important to interpret the comparisons in this paper, and this analysis could also be a useful reference for assimilative models which will ingest thermospheric wind data. Such models often have an explicit or implicit notion of data covariance or correlation functions, the spatial distribution of which can be informed by the discussion below.

Because most geophysical observations can be represented as a spatial or temporal average of the true underlying quantity, they can usually be written as a Fredholm integral of the first kind:

$$g(x) = \int h(s, x) f(s)\, \mathrm{d}s \tag{A1}$$

where f is the true quantity being observed, x and s may be multi-dimensional, representing time and/or space, g is an imperfect observation of f, and h is a spatial and/or temporal averaging function, usually referred to as an impulse response or averaging kernel. In the case where h depends only on $s - x$, this equation reduces to convolution. Noise is neglected but can be trivially included as an additive term.

Per the Nyquist sampling theorem, the smallest resolvable scale is twice the width of the averaging kernel, h. In order to compare averaging kernels with different shapes, we define the width by considering the second central moment of h:

$$\sigma^2 = \int_{-\infty}^{\infty} (x - \mu_h)^2\, h(x)\, \mathrm{d}x \tag{A2}$$

where h is defined to be normalized such that it integrates to 1, and μ_h is the first moment of h. For example, the width of a rectangle function is 3.46σ and the full width at half-maximum of a Gaussian function is 2.36σ. Different definitions of "width" are useful for different purposes. For simplicity, here we define the width of h as 2σ, though the normalization is unimportant for this study since we are interested in relative differences between MIGHTI and SMR.

For a specular meteor radar using the homogeneous velocity technique, the averaging kernel can be defined analytically for a known meteor echo distribution:

$$h_{i,\mathrm{SMR}}(x) \propto n(x)\, b_i(x) \tag{A3}$$

where $n(x)$ is the density of meteors detected at location x, i can represent the zonal or meridional wind, and b_i is the component of the Bragg vector in the direction of i. Using the average meteor distribution in one day of Tirupati data, we evaluate the expressions above. For the zonal wind, the zonal width is $2\sigma = 260$ km and the meridional width

Table A1. Horizontal Averaging Kernels for ICON-MIGHTI and specular meteor radar (SMR)

Case	2σ width	Direction
SMR	190–290 km	All
MIGHTI field of view	75 km	Across LoS
MIGHTI exposure time	125 km (Day) 250 km (Night)	Along spacecraft velocity
MIGHTI ray path length	760–1200 km (Day) 220–450 km (Night)	Along LoS

is 210 km. The meridional wind is similar, with a meridional width of 290 km and a zonal width of 190 km.

For MIGHTI, three main factors contribute to the horizontal averaging kernel. First, the horizontal field of view is 2.7°, which equates to an averaging kernel with $2\sigma = 75$ km in the direction across the line of sight. Second, the 7.1 km/s spacecraft velocity in the Earth-fixed frame implies an averaging kernel with a width of $2\sigma = 125$ km during the day and 250 km at night.

The third factor is the averaging along the line of sight, which the most important yet most difficult to quantify, as it depends on the airglow distribution and the inversion technique. In the case where h depends only on $s-x$, the averaging kernel is equal to the observation $g(x)$ when the true quantity $f(x)$ is a delta function. Here we determine this via simulation. In practice, we first compute the integral of h by simulating $g(x)$ when $f(x)$ is a step function, then differentiate to obtain h. The simulation used is detailed Section 4 of Harding et al. (2017). In brief, given a known airglow and wind distribution, a forward model simulates the observed interferogram. This interferogram is processed with the Level 1 and Level 2.1 MIGHTI algorithms to produce an observed wind. By sweeping the location of the discontinuity in $f(x)$, we trace out the shape of $g(x)$, and then differentiate to obtain $h(x)$. In general each altitude has its own averaging kernel. We simulate day and night separately. In each, a representative solar-minimum, equinoctial, equatorial green-line emission profile is used, similar to the profiles in Fig 7 of Harding et al. (2017). The emission rate and wind are spherically symmetric except for the step-function discontinuity in the wind.

Applying (A2) to the computed averaging kernel $h(x)$, we find that at night, the along-LoS averaging kernel has a 2σ width of $220-450$ km, whereas during the day it is much larger, $760-1200$ km. The width is larger at lower altitudes, where the path length through the layer gets longer. It is noted that this quantitative result depends on the MIGHTI processing technique. More advanced techniques such as the one described by Y. J. Wu et al. (2020), or possibly tomographic techniques, may be able to improve the resolution.

The 2σ averaging kernel widths described in this Appendix are summarized in Table A1.

Acknowledgments

The line of sight winds and metadata from all 1158 MIGHTI-SMR coincidences are archived on Zenodo (http://doi.org/10.5281/zenodo.4050607). This analysis used v03 of the Level 2.1 ICON-MIGHTI data, which is available from the ICON website (https://icon.ssl.berkeley.edu/Data) and will soon be available at the Space Physics Data Facility (https://spdf.gsfc.nasa.gov/). The Ledong, Wuhan and Beijing meteor radars are supported by the NSFC (41727803), the Solar-Terrestrial Environment Research Network of Chinese Academy of Sciences, and the Chinese Meridian Project. The meteor wind data from Ledong, Wuhan and Beijing are archived at the Data Center for Geophysics (http://wdc.geophys.ac.cn/), National Earth System Science Data Sharing Infrastructure at BNOSE, IGGCAS. The Tirupati meteor radar dataset used here is available on Zenodo (https://doi.org/10.5281/zenodo.4433180). The authors are grateful to the broader ICON team. ICON is supported by NASA's Explorers Program through contracts NNG12FA45C and NNG12FA42I. The participation of JLC and MH in this work is part of the project supported by the Deutsche Forschungsgemeinschaft (DFG, German Research Foundation) under SPP 1788 (DynamicEarth)-CH 1482/1-2 (DYNAMITE2).

References

Burrage, M. D., Skinner, W. R., Gell, D. A., Hays, P. B., Marshall, A. R., Ortland, D. A., ... Vincent, R. A. (1996). Validation of mesosphere and lower thermosphere winds from the high resolution Doppler imager on UARS. *Journal of Geophysical Research: Atmospheres*, *101*(D6), 10365–10392. Retrieved from `http://doi.wiley.com/10.1029/95JD01700` doi: 10.1029/95JD01700

Chau, J. L., Urco, J. M., Vierinen, J., Andrew Volz, R., Clahsen, M., Pfeffer, N., & Trautner, J. (2019). Novel specular meteor radar systems using coherent MIMO techniques to study the mesosphere and lower thermosphere. *Atmospheric Measurement Techniques*, *12*(4), 2113–2127. doi: 10.5194/amt-12-2113-2019

Drob, D. P., Emmert, J. T., Meriwether, J. W., Makela, J. J., Doornbos, E., Conde, M. G., ... Klenzing, J. H. (2015). An update to the Horizontal Wind Model (HWM): The quiet time thermosphere. *Earth and Space Science*, *2*(7), 301–319. Retrieved from `http://doi.wiley.com/10.1002/2014EA000089` doi: 10.1002/2014EA000089

England, S. L. (2011). A review of the effects of non-migrating atmospheric tides on the Earth's low-latitude ionosphere. *Space Science Reviews*, *168*(1-4), 211–236. Retrieved from `http://link.springer.com/10.1007/s11214-011-9842-4` doi: 10.1007/s11214-011-9842-4

Englert, C. R., Harlander, J. M., Brown, C. M., Marr, K. D., Miller, I. J., Stump, J. E., ... Immel, T. J. (2017). Michelson Interferometer for Global High-Resolution Thermospheric Imaging (MIGHTI): Instrument Design and Calibration. *Space Science Reviews*, *212*(1-2), 553–584. Retrieved from `http://dx.doi.org/10.1007/s11214-017-0358-4http://link.springer.com/10.1007/s11214-017-0358-4` doi: 10.1007/s11214-017-0358-4

Forbes, J. M., Portnyagin, Y. I., Skinner, W., Vincent, R. A., Solovjova, T., Merzlyakov, E., ... Palo, S. (2004). Climatological lower thermosphere winds as seen by ground-based and space-based instruments. *Annales Geophysicae*, *22*(6), 1931–1945. doi: 10.5194/angeo-22-1931-2004

Fuller-Rowell, T. J. (2011). Storm-time response of the thermosphere-ionosphere system. In M. A. Abdu & D. Pancheva (Eds.), *Aeronomy of the earth's atmosphere and ionosphere* (pp. 419–435). Dordrecht: Springer Netherlands. Retrieved from `http://link.springer.com/10.1007/978-94-007-0326-1` doi: 10.1007/978-94-007-0326-1

Harding, B. J., Makela, J. J., Englert, C. R., Marr, K. D., Harlander, J. M., England, S. L., & Immel, T. J. (2017). The MIGHTI Wind Retrieval Algorithm: Description and Verification. *Space Science Reviews*, *212*(1-2), 585–600. Retrieved from `http://dx.doi.org/10.1007/s11214-017-0359-3http://link.springer.com/10.1007/s11214-017-0359-3` doi: 10.1007/s11214-017-0359-3

Harlander, J. M., Englert, C. R., Brown, C. M., Marr, K. D., Miller, I. J., Zastera, V., ... Mende, S. B. (2017). Michelson Interferometer for Global High-Resolution Thermospheric Imaging (MIGHTI): Monolithic Interferometer Design and Test. *Space Science Reviews*, *212*(1-2), 601–613. Retrieved from `http://dx.doi.org/10.1007/s11214-017-0358-4` doi:

10.1007/s11214-017-0374-4

Hays, P. B., Abreu, V. J., Dobbs, M. E., Gell, D. A., Grassl, H. J., & Skinner, W. R. (1993). The high-resolution Doppler imager on the upper atmosphere research satellite. *Journal of Geophysical Research*, *98*(D6). doi: 10.1029/93jd00409

Hays, P. B., Killeen, T. L., & Kennedy, C. (1981). The Fabry-Perot Interferometer on Dynamics Explorer. *Space Science Instrumentation*, *5*, 395–416.

Heelis, R. (2004). Electrodynamics in the low and middle latitude ionosphere: A tutorial. *Journal of Atmospheric and Solar-Terrestrial Physics*, *66*(10), 825–838. Retrieved from `http://linkinghub.elsevier.com/retrieve/pii/S1364682604000525` doi: 10.1016/j.jastp.2004.01.034

Holdsworth, D. A., Reid, I. M., & Cervera, M. A. (2004). Buckland park all-sky interferometric meteor radar. *Radio Science*, *39*(5). doi: 10.1029/2003RS003014

Hysell, D. L., Larsen, M. F., & Sulzer, M. P. (2014). High time and height resolution neutral wind profile measurements across the mesosphere/lower thermosphere region using the Arecibo incoherent scatter radar. *Journal of Geophysical Research: Space Physics*, *119*(3), 2345–2358. Retrieved from `http://doi.wiley.com/10.1002/2013JA019621` doi: 10.1002/2013JA019621

Immel, T. J., England, S. L., Mende, S. B., Heelis, R. A., Englert, C. R., Edelstein, J., . . . Sirk, M. M. (2017, 2). The Ionospheric Connection Explorer Mission: Mission Goals and Design. *Space Science Reviews*, *214*(13). Retrieved from `http://dx.doi.org/10.1007/s11214-017-0449-2http://link.springer.com/10.1007/s11214-017-0449-2` doi: 10.1007/s11214-017-0449-2

Killeen, T. L. (1987). Energetics and dynamics of the Earth's thermosphere. *Reviews of Geophysics*, *25*(3), 433. Retrieved from `http://doi.wiley.com/10.1029/RG025i003p00433` doi: 10.1029/RG025i003p00433

Killeen, T. L., Wu, Q., Solomon, S. C., Ortland, D. A., Skinner, W. R., Niciejewski, R. J., & Gell, D. A. (2006). TIMED Doppler Interferometer: Overview and recent results. *Journal of Geophysical Research: Space Physics*, *111*(10), 1–19. doi: 10.1029/2005JA011484

Larsen, M. F. (2002). Winds and shears in the mesosphere and lower thermosphere: Results from four decades of chemical release wind measurements. *Journal of Geophysical Research*, *107*(A8), 1215. Retrieved from `http://doi.wiley.com/10.1029/2001JA000217http://doi.wiley.com/10.1029/2001JA000218` doi: 10.1029/2001JA000218

Liu, H. L. (2016). Variability and predictability of the space environment as related to lower atmosphere forcing. *Space Weather*, *14*(9), 634–658. doi: 10.1002/2016SW001450

Makela, J. J., Baughman, M., Navarro, L. A., Harding, B. J., Englert, C. R., Harlander, J. M., . . . Immel, T. J. (2020, 12). Validation of ICON-MIGHTI thermospheric wind observations: 1. Nighttime Red-line Ground-Based Fabry-Perot Interferometers. *Journal of Geophysical Research: Space Physics*, 1–29. Retrieved from `https://onlinelibrary.wiley.com/doi/10.1029/2020JA028726` doi: 10.1029/2020JA028726

Marr, K. D., Morrow, W. H., Brown, C. M., Englert, C. R., Harlander, J. M., & Cerrato, A. (2019). Calibration lamp design, characterization, and implementation for the Michelson Interferometer for Global High-Resolution Thermospheric Imaging instrument on the Ionospheric Connection satellite. *Optical Engineering*, *58*(05), 1. doi: 10.1117/1.OE.58.5.054104

Marr, K. D., Thayer, A. S., Englert, C. R., & Harlander, J. M. (2020). Determining the thermomechanical image shift for the MIGHTI instrument on the NASA-ICON satellite. *Optical Engineering*, *59*(01), 1. doi: 10.1117/1.oe.59.1.013102

Maute, A., Richmond, A. D., & Roble, R. G. (2012). Sources of low-latitude ionospheric E x B drifts and their variability. *Journal of Geophysical Research:*

Space Physics, *117*(6), 1–14. doi: 10.1029/2011JA017502

Meriwether, J. W. (2006). Studies of thermospheric dynamics with a Fabry-Perot interferometer network: A review. *Journal of Atmospheric and Solar-Terrestrial Physics*, *68*(13), 1576–1589. Retrieved from `http://linkinghub.elsevier.com/retrieve/pii/S1364682606001192` doi: 10.1016/j.jastp.2005.11.014

Pedatella, N. M., Lu, G., & Richmond, A. D. (2018). Effects of High-Latitude Forcing Uncertainty on the Low-Latitude and Midlatitude Ionosphere. *Journal of Geophysical Research: Space Physics*, 1–21. Retrieved from `http://doi.wiley.com/10.1002/2017JA024683` doi: 10.1002/2017JA024683

Rao, S. V. B., Eswaraiah, S., Venkat Ratnam, M., Kosalendra, E., Kishore Kumar, K., Sathish Kumar, S., ... Gurubaran, S. (2014). Advanced meteor radar installed at tirupati: System details and comparison with different radars. *Journal of Geophysical Research: Atmospheres*, *119*(21), 11,893-11,904. doi: 10.1002/2014JD021781

Richmond, A. D. (2011). Electrodynamics of Ionosphere-Thermosphere Coupling. In *Aeronomy of the earth's atmosphere and ionosphere* (pp. 191–201). doi: 10.1007/978-94-007-0326-1

Rishbeth, H. (1972). Thermospheric winds and the F-region: A review. *Journal of Atmospheric and Terrestrial Physics*, *34*(1972), 1–47.

Shepherd, G. G., Thuillier, G., Cho, Y.-M., Duboin, M.-L., Evans, W. F. J., Gault, W. A., ... Ward, W. E. (2012). The Wind Imaging Interferometer (WINDII) on the Upper Atmosphere Research Satellite: A 20 year perspective. *Reviews of Geophysics*, *50*(2), RG2007. Retrieved from `http://doi.wiley.com/10.1029/2012RG000390` doi: 10.1029/2012RG000390

Stevens, M. H., Englert, C. R., Harlander, J. M., England, S. L., Marr, K. D., Brown, C. M., & Immel, T. J. (2018). Retrieval of Lower Thermospheric Temperatures from O2 A Band Emission: The MIGHTI Experiment on ICON. *Space Science Reviews*, *214*(1). Retrieved from `http://dx.doi.org/10.1007/s11214-017-0434-9` doi: 10.1007/s11214-017-0434-9

Titheridge, J. (1995). Winds in the ionosphere - A review. *Journal of Atmospheric and Terrestrial Physics*, *57*(14), 1681–1714. Retrieved from `http://linkinghub.elsevier.com/retrieve/pii/002191699500091F` doi: 10.1016/0021-9169(95)00091-F

Vierinen, J., Chau, J. L., Charuvil, H., Urco, J. M., Clahsen, M., Avsarkisov, V., ... Volz, R. (2019). Observing Mesospheric Turbulence With Specular Meteor Radars: A Novel Method for Estimating Second-Order Statistics of Wind Velocity. *Earth and Space Science*, *6*(7), 1171–1195. doi: 10.1029/2019EA000570

Visser, T., March, G., Doornbos, E., Visser, C., & Visser, P. (2019). Characterization of Thermospheric Vertical Wind Activity at 225—295 km Altitude Using GOCE Data and Validation Against Explorer Missions. *Journal of Geophysical Research: Space Physics*, 2019JA026568. Retrieved from `https://onlinelibrary.wiley.com/doi/abs/10.1029/2019JA026568` doi: 10.1029/2019JA026568

Wang, Y., Li, G., Ning, B., Yang, S., Sun, W., & Yu, Y. (2019). All-sky interferometric meteor radar observations of zonal structure and drifts of low-latitude ionospheric e region irregularities. *Earth and Space Science*, *6*(12), 2653-2662. doi: 10.1029/2019EA000884

Wu, Q., Killeen, T. L., Ortland, D. A., Solomon, S. C., Gablehouse, R. D., Johnson, R. M., ... Franke, S. J. (2006). TIMED Doppler interferometer (TIDI) observations of migrating diurnal and semidiurnal tides. *Journal of Atmospheric and Solar-Terrestrial Physics*, *68*(3-5), 408–417. doi: 10.1016/j.jastp.2005.02.031

Wu, Y. J., Harding, B. J., Triplett, C. C., Makela, J. J., Marr, K. D., Englert, C. R.,

... Immel, T. J. (2020). Errors from asymmetric emission rate in spaceborne, limb sounding Doppler interferometry: A correction algorithm with application to ICON/MIGHTI. *Earth and Space Science*. doi: 10.1029/2020ea001164

Xiong, C., Lühr, H., & Fejer, B. G. (2015). Global features of the disturbance winds during storm time deduced from CHAMP observations. *Journal of Geophysical Research A: Space Physics*, *120*(6), 5137–5150. doi: 10.1002/2015JA021302

Yu, Y., Wan, W., Ning, B., Liu, L., Wang, Z., Hu, L., & Ren, Z. (2013). Tidal wind mapping from observations of a meteor radar chain in december 2011. *Journal of Geophysical Research: Space Physics*, *118*(5), 2321-2332. doi: 10.1029/2012JA017976